

Optimization of Phase-Engineered a-Si:H- Based Multijunction Solar Cells

C. R. Wronski, R. W. Collins,

J. Deng, J. Pearce, X. Niu, M. Albert, G. M. Ferreira, C. Chen, N. Podraza

**Center for Thin Film Devices
The Pennsylvania State University
University Park, PA 16802**

**Quarterly Technical Status Report
April 2004 – August 2004**

Subcontract No. NDJ-1-30630-01

NREL Technical Monitor: Bolko von Roedern

Table of Contents

Table of Contents	2
Executive Summary	3
Task 1: Materials Research and Device Development	3
Task 3: Device Loss Mechanisms.....	3
Task 4: Characterization Strategies for Advanced Materials	4
Task 1: Materials Research and Device Development	6
Task 3: Device loss mechanisms	23
Task 4: Characterization Strategies for Advanced Materials	28

Executive Summary

Task 1: Materials Research and Device Development

There is considerable motivation for establishing a better understanding of the growth processes for $\text{a-Si}_{1-x}\text{Ge}_x\text{:H}$ alloys. This may be possible through the application of real time spectroscopic ellipsometry (RTSE) to the development of deposition phase diagrams for $\text{a-Si}_{1-x}\text{Ge}_x\text{:H}$. With this approach, directions for possible improvements to existing world-record performance a-Si:H -based solar cells can be suggested.. A study has been undertaken that involves multiple deposition parameter scans to understand the role of substrate temperature, gas pressure, and plasma frequency on the physical processes of surface diffusion, the ultimate ordering in the film, and crystallite nucleation from the amorphous phase. In the approach applied for this study, guidance is being obtained into the optimization of complicated film growth processes using the deposition phase diagram concept. Phase engineering of the intrinsic semiconductor materials was carried out to obtain improvements in $\text{Si}_{1-x}\text{Ge}_x\text{:H}$ and to understand the phase transitions for these films. The insights obtained from these studies are being applied to optimize $\text{Si}_{1-x}\text{Ge}_x\text{:H}$ solar cell structures. Results have been obtained which include the first two phase diagrams for $\text{Si}_{1-x}\text{Ge}_x\text{:H}$ materials, prepared at different temperatures. Other deposition parameters are being explored which include gas pressure and flows in an attempt to retain the stable surface growth mode of $\text{Si}_{1-x}\text{Ge}_x\text{:H}$ at higher rates.

Task 3: Device Loss Mechanisms

The studies on a-Si:H solar cells have continued to address the mechanisms and defect states determining their characteristics using the powerful and sensitive techniques based on

J_D -V characteristics. The predictions from the analytical model previously described have been verified and self-consistent interpretation of a wide range of these characteristics in highly controlled cell structures is being continued. The “differential diode quality factors”, $n(V)$, resulting from bulk recombination in the i-layers are being further characterized in order to obtain information about the distributions of gap states in different i-layer materials and their evolution during light and forward bias induced degradation. The ability to create in a controlled way metastable defects in the i-layers with carrier recombination under forward bias and the equivalence between this and the corresponding creation with illumination has been further established. Advantage is being taken of this in characterizing the kinetics of the metastable defect state creation and subsequent relaxation directly with J_D -V characteristics. This is being applied in the studies on the fast and slow state creation obtained with different carrier recombination rates and the kinetics of their subsequent relaxation in order to directly identify separate and quantify the contributions of “light annealing”. The J_D -V characteristics of solar cell structures having different thickness supplied by United Solar Ovonic have been investigated. No thickness dependence of the characteristics on these “non-optimized” i-layer cells could be found in part due to their thickness variations and shunting problems. The cell geometries used in the Penn State studies are being fabricated on solar cells supplied by them for i-layers that have been optimized for a given thickness.

Task 4: Characterization Strategies for Advanced Materials

Studies are continuing on both diluted and undiluted a-Si:H thin films of the evolution of light induced defect states under 1 sun illumination and their subsequent relaxation. An experimental station has been constructed with precise control of the sample temperatures as

well as the intensities of volume absorbed illumination for adjusting the quasi-Fermi level splitting of the photoconductivities used in characterizing both the degradation as well as its relaxation. In addition, automation of the experimental procedures enhances the precision of the measurements as well as their reproducibility.

Task 1: Materials Research and Device Development

Comparison of Si:H and Si_{1-x}Ge_x:H at Low Pressure and Low Power

The Si_{1-x}Ge_x:H films studied for phase diagram development were deposited on native-oxide/c-Si using single-chamber rf PECVD and were measured in real time using a rotating-compensator multichannel ellipsometer. Conditions similar to those used for optimum pure a-Si:H were adopted, including a relatively low substrate temperature ($T = 200^\circ\text{C}$), the minimum plasma power possible for a stable plasma (0.08 mW/cm^2), a low partial pressure of $[\text{SiH}_4] + [\text{GeH}_4]$ (0.03-0.09 Torr), and a total pressure of less than 1.0 Torr. The flow ratio $G = [\text{GeH}_4] / \{[\text{SiH}_4] + [\text{GeH}_4]\}$ was fixed at $G = 0.167$, in an attempt to obtain a room-temperature gap of $\sim 1.4 \text{ eV}$ for use of the resulting a-Si_{1-x}Ge_x:H as the i-layer of the bottom solar cell of the triple junction device.

Figure 1 compares the deposition rates of the similarly-prepared a-Si:H and a-Si_{1-x}Ge_x:H. The significantly higher rates for the alloys are attributed to the ease with which GeH₄ in the plasma is dissociated relative to SiH₄. Figure 2 depicts the evolution of the surface roughness layer thickness versus bulk layer thickness in separate panels for selected films that remain amorphous throughout growth, i.e., for $R = [\text{H}_2] / \{[\text{SiH}_4] + [\text{GeH}_4]\} = 15, 40, \text{ and } 60$. The microstructural evolution is shown in Figure 3 for films that nucleate in the amorphous phase and exhibit an $a \rightarrow (a + \mu c)$ transition, i.e., for $R = 75, 80, \text{ and } 100$.

Figure 4 shows the deposition phase diagrams of the pure Si:H and the Si_{1-x}Ge_x:H alloy thin films deduced from the data of Figures 2 and 3. Two significant differences are observed between the two diagrams, indicating the profound effect of alloying. First, the $a \rightarrow (a + \mu c)$ transition for the series of Si_{1-x}Ge_x:H alloys is shifted to much larger R compared to pure Si:H.

Thus, the presence of Ge in the growth process suppresses the nucleation of microcrystals from the amorphous phase. Second, the $a \rightarrow a$ roughening transition saturates at a very low layer thickness of 200 Å, even as the $a \rightarrow (a+\mu c)$ transition for thick films is approached and crossed. In contrast for Si:H, the $a \rightarrow a$ roughening transition increases sharply, exceeding the bulk layer thickness of 4000 Å, as the $a \rightarrow (a+\mu c)$ transition is approached. This comparison demonstrates that the average diffusion length of precursors on the film surface during growth is significantly reduced for the alloys, likely due to surface defects. Furthermore, it also suggests that no significant gain in the device performance of these alloys can be realized by increasing the hydrogen dilution up to the $a \rightarrow (a+\mu c)$ transition for the layer thickness desired in the device.

Finally, Figure 5 shows the optical band gap E_g determination for the film of Figure 2 with $R=15$. This is performed via an extrapolation of $\epsilon_2^{1/2}$ versus photon energy E over the lowest energy range. The imaginary part of the dielectric function ϵ_2 is deduced by inversion using the $\Sigma\sigma$ -minimization criterion to identify the proper values of d_s and d_b (An *et al.*, 1991). The bulk layer thickness corresponding to the inverted result in Fig. 6.5 was near 200 Å. The optical band gap of $E_g=1.26$ eV was deduced in Fig. 6.5 for the measurement temperature of 200°C. If one were to apply the slope of the observed linear temperature dependence of the optical band gap for a-Si:H, -5×10^{-4} eV/K, then a room temperature gap of 1.35 eV would be predicted.

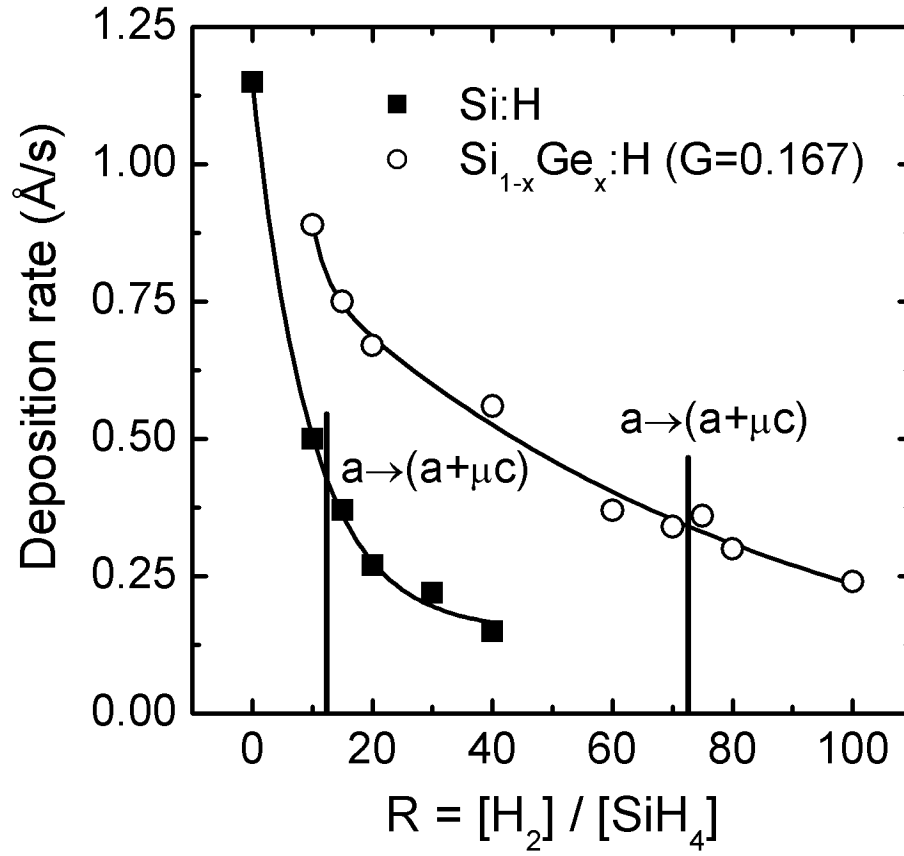


Figure 1: A comparison of the deposition rates of pure Si:H and Si_{1-x}Ge_x:H films prepared as a function of the H₂-dilution ratio R. For both series, the substrate temperature was 200°C, the plasma power was 0.08 mW/cm², and the reactive gas partial pressure was between 0.03 and 0.09 Torr.

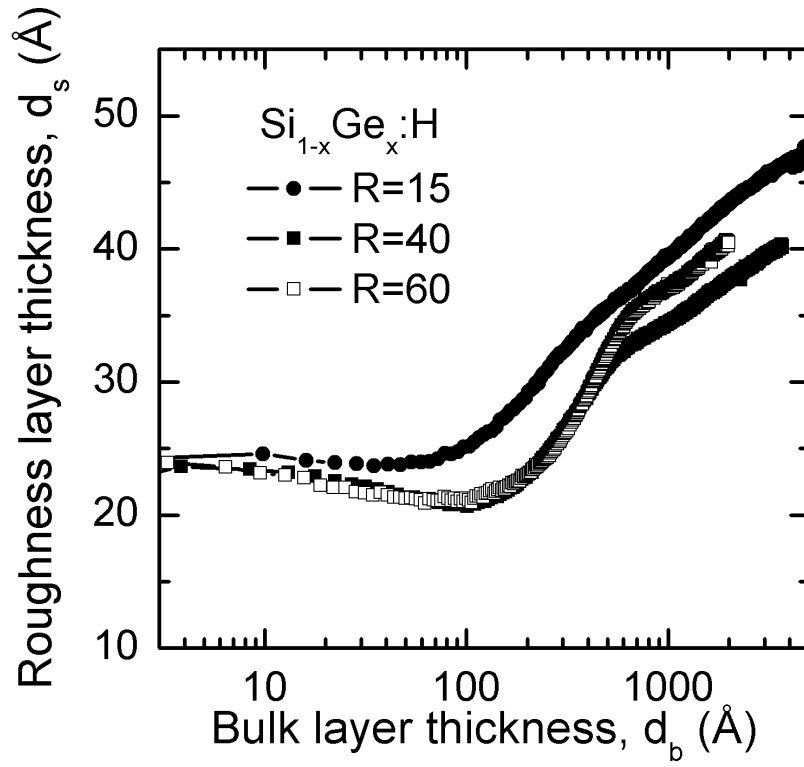


Figure 2: Surface roughness layer thickness versus bulk layer thickness for $\text{Si}_{1-x}\text{Ge}_x\text{:H}$ films with $R = 15, 40$, and 60 that grow in the amorphous phase throughout the deposition process. For this series of films, the substrate temperature was 200°C , the plasma power was 0.08 mW/cm^2 , and the reactive gas partial pressure was between 0.03 and 0.09 Torr.

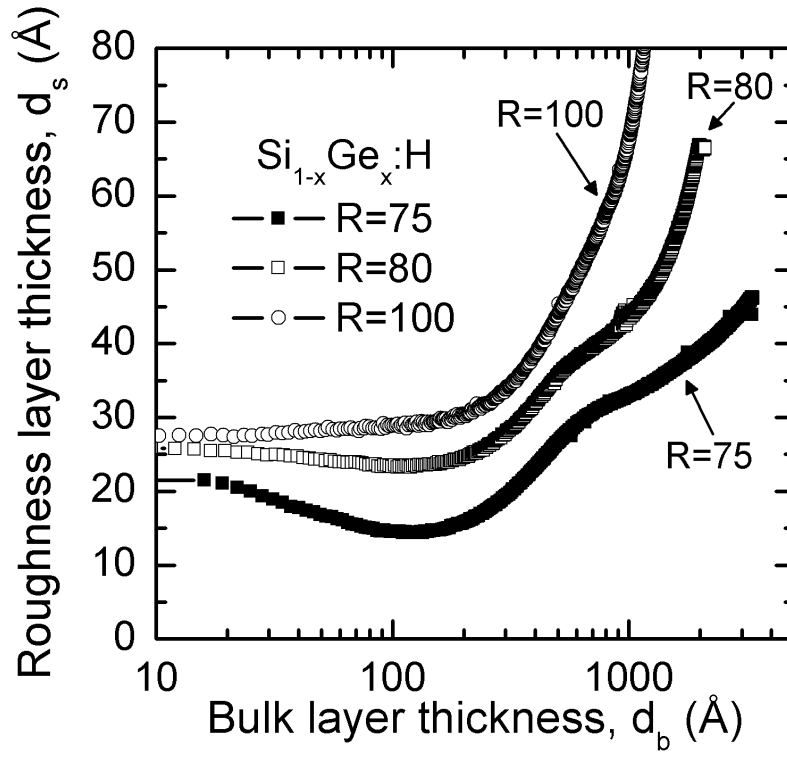


Figure 3: Surface roughness layer thickness versus bulk layer thickness for $\text{Si}_{1-x}\text{Ge}_x\text{:H}$ films with $R = 75, 80$, and 100 that nucleate in the amorphous phase but evolve to the microcrystalline phase with increasing thickness. For this series, the substrate temperature was 200°C , the plasma power was 0.08 mW/cm^2 , and the reactive gas partial pressure was between 0.03 and 0.09 Torr.

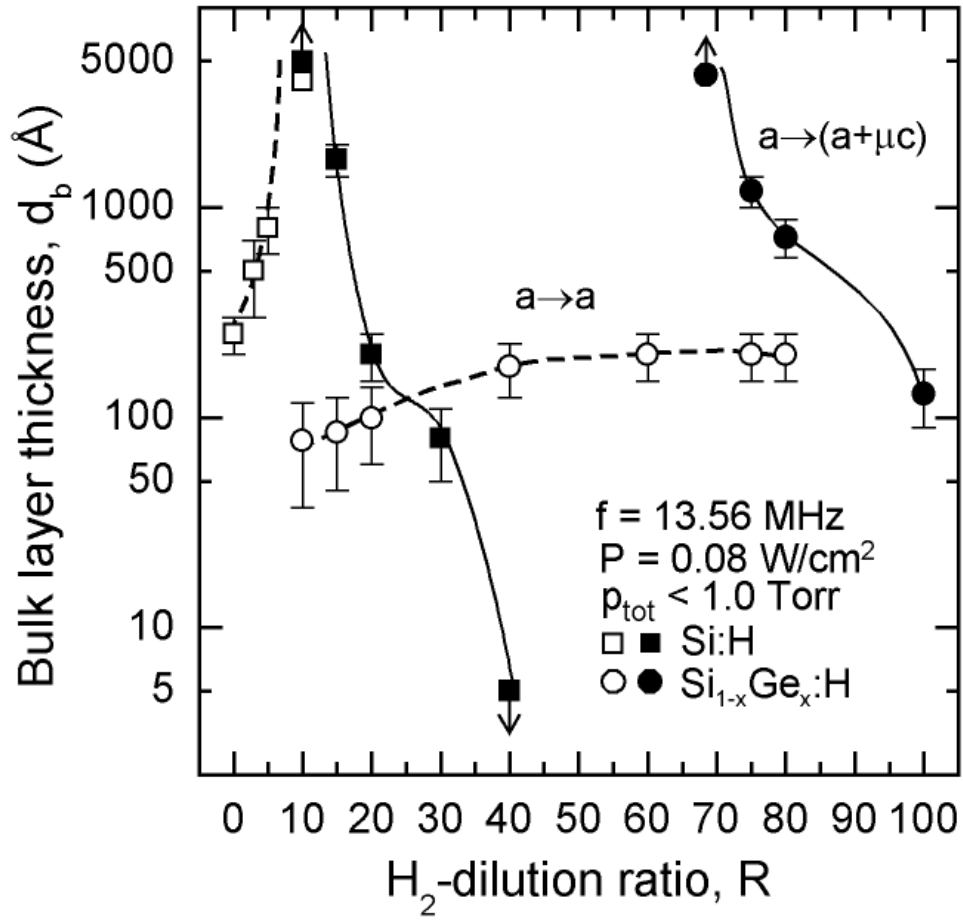


Figure 4: Superimposed phase diagrams for the $Si:H$ (squares) and $Si_{1-x}Ge_x:H$ (circles) films deposited at low power (0.08 mW/cm²) and low total pressure (< 1.0 Torr) on native oxide-covered c-Si substrates held at 200°C . The (up, down) arrows indicate that the transition occurs (above, below) the designated value.

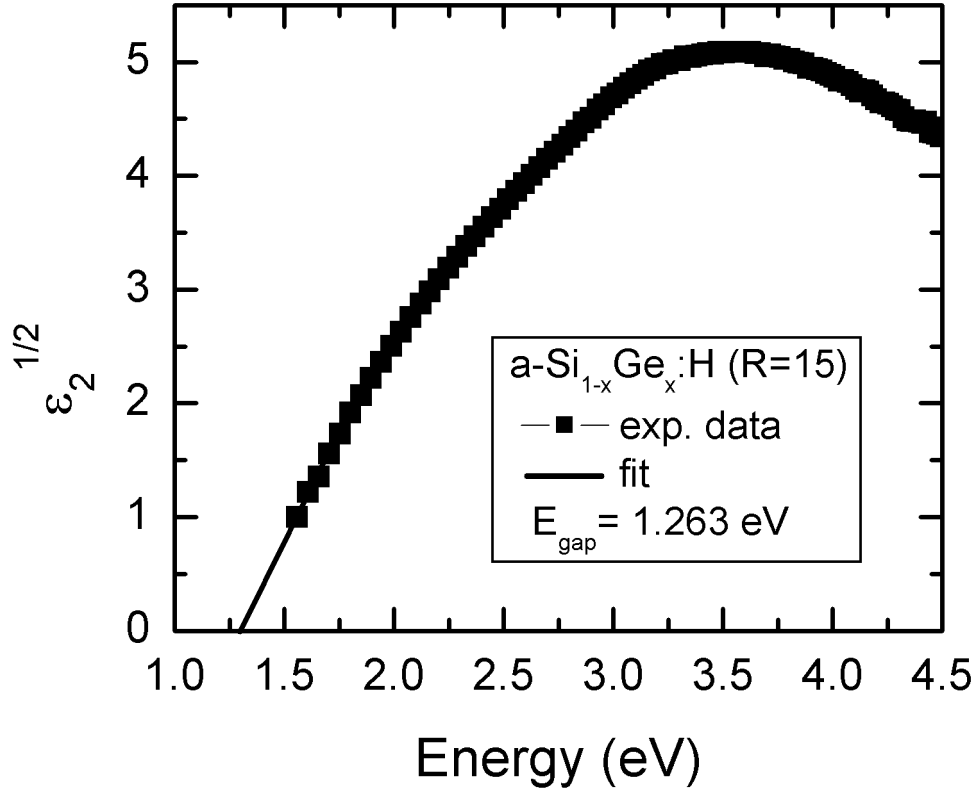


Figure 5: Optical band gap plot consisting of $\epsilon_2^{1/2}$ versus photon energy over the lowest energy range, extrapolated to zero ordinate. This approach for determining the gap is based on the assumption of parabolic valence and conduction bands, a constant dipole matrix element, and no absorption below the optical band gap E_g .

Comparison of $\text{Si}_{1-x}\text{Ge}_x\text{:H}$ at Different Substrate Temperature

Figure 6 shows the deposition rates for the series of $\text{Si}_{1-x}\text{Ge}_x\text{:H}$ films from Figure 1, along with those for a series of films prepared similarly, including (i) the minimum plasma power possible for a stable plasma (0.08 mW/cm^2), (ii) a low partial pressure of $[\text{SiH}_4] + [\text{GeH}_4]$ ($0.03\text{--}0.09 \text{ Torr}$), (iii) a total pressure of less than 1.0 Torr , and (iv) a flow ratio $G = [\text{GeH}_4] / \{[\text{SiH}_4] + [\text{GeH}_4]\}$ fixed at $G=0.167$. The only differences for the new set of series in Figure 6 are substrate temperatures of 260°C , 290°C , and 320°C , compared with 200°C for the

series of Figure 1. The comparison in Figure 6 demonstrates that the high temperature series exhibits a slightly higher deposition rate, as would be expected if the incorporation of precursors into the $\text{Si}_{1-x}\text{Ge}_x\text{:H}$ network is weakly activated.

Figure 7 depicts the evolution of the surface roughness thickness (d_s) versus the bulk layer thickness (d_b) for those $\text{Si}_{1-x}\text{Ge}_x\text{:H}$ films prepared at 260°C that remain amorphous throughout the deposition ($R=15, 40$, and 60). It is clear that the smoothening effect during the initial stages of film growth is much larger for this series of films compared with the results for the lower temperature series of Figure 2. Figure 8 shows the corresponding results for the films of the 260°C series that nucleate in the amorphous phase and exhibit an $a \rightarrow (a+\mu c)$ transition, i.e., for films with $R=70, 80$, and 100 . Finally, Figure 9 shows an atomic force microscopy image for the $\text{Si}_{1-x}\text{Ge}_x\text{:H}$ film of Figure 8 with $R=80$ that evolves from amorphous to mixed-phase (amorphous+microcrystalline) Si:H during the deposition. The larger bright clusters are interpreted as crystallites that extend above the surrounding amorphous phase surface.

In order to summarize the effect of temperature on the growth of $\text{Si}_{1-x}\text{Ge}_x\text{:H}$, Fig. 10 shows the deposition phase diagrams of the $\text{Si}_{1-x}\text{Ge}_x\text{:H}$ alloy thin films for both temperatures ($T=200^\circ\text{C}$ and 260°C). Significant differences can be observed between the two diagrams. First, the $a \rightarrow (a+\mu c)$ transition for the $T=260^\circ\text{C}$ series of $\text{Si}_{1-x}\text{Ge}_x\text{:H}$ alloys is shifted to smaller R compared to the lower temperature series. Second, the $a \rightarrow a$ roughening transition increases moderately for all the films prepared at higher temperature. Third, the $a \rightarrow (a+\mu c)$ transition for highly diluted films ($R=70, 80$, and 100) is reduced. Moreover, the film deposited with $T=260^\circ\text{C}$ and $R=100$ is unique in that it evolves through three phases: amorphous, mixed-phase and single-phase microcrystalline.

Figure 11 depicts the evolution of the surface roughness thickness (d_s) versus the bulk layer thickness (d_b) for those $\text{Si}_{1-x}\text{Ge}_x\text{:H}$ films prepared at 290°C that remain amorphous throughout the deposition ($R=40$ and 50). It is clear that the smoothening effect during the initial stages of film growth is much larger for this series of films compared with the results for the lower temperature series of Figures 2 and 7. Figure 12 shows the corresponding results for the films of the 290°C series that nucleate in the amorphous phase and exhibit an $a \rightarrow (a+\mu c)$ transition, i.e., for films with $R=60, 80$, and 100 .

Figure 13 depicts the evolution of the surface roughness thickness (d_s) versus the bulk layer thickness (d_b) for those $\text{Si}_{1-x}\text{Ge}_x\text{:H}$ films prepared at 320°C that remain amorphous throughout the deposition ($R=0, 5, 10, 20, 40, 60$, and 80). It is clear that the smoothening effect during the initial stages of film growth is much larger for this series of films compared with the results for the lower temperature series of Figure 2, 7 and 11. No films from this series nucleate in the amorphous phase and exhibit an $a \rightarrow (a+\mu c)$ transition similar to those films deposited at $T=200^\circ\text{C}, 260^\circ\text{C}$, and 290°C .

In summary, increasing the substrate temperature for $\text{Si}_{1-x}\text{Ge}_x\text{:H}$ films deposited at low power and at low pressure leads to beneficial results on the film growth process due to the enhancement of the diffusion of precursors. Thus, there is an enhancement in the surface smoothening during nuclei coalescence in the amorphous growth regime, leading to a smoother surface in the stable surface regime. Finally, the higher temperature are expected to lead to improved device properties for the $a\text{-Si}_{1-x}\text{Ge}_x\text{:H}$.

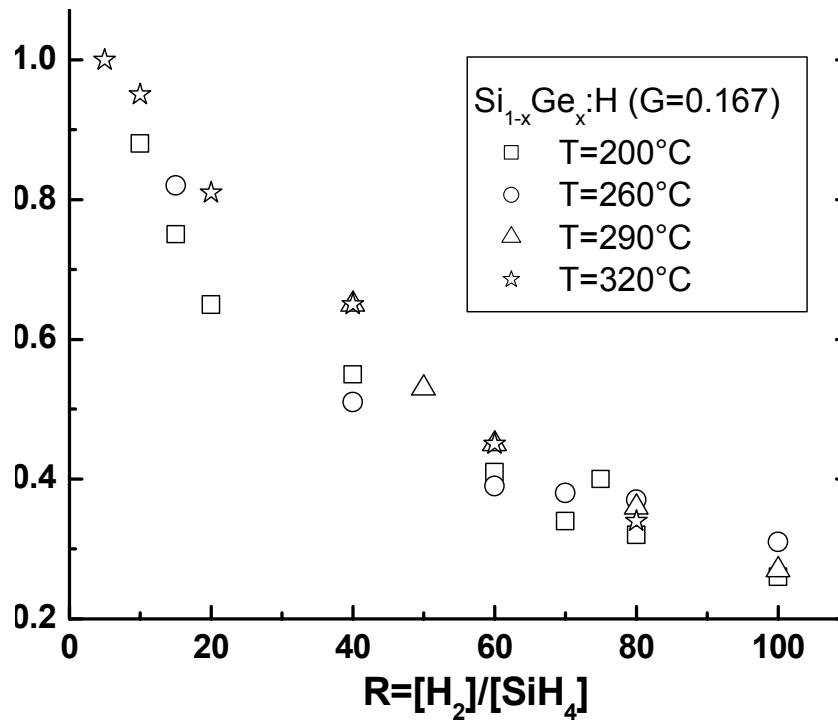


Figure 6: A comparison of the deposition rates as a function of the H₂-dilution ratio R for Si_{1-x}Ge_x:H films prepared at different substrate temperatures: 200°C (squares); 260°C (circles); 290°C (triangles); and 320°C (stars).

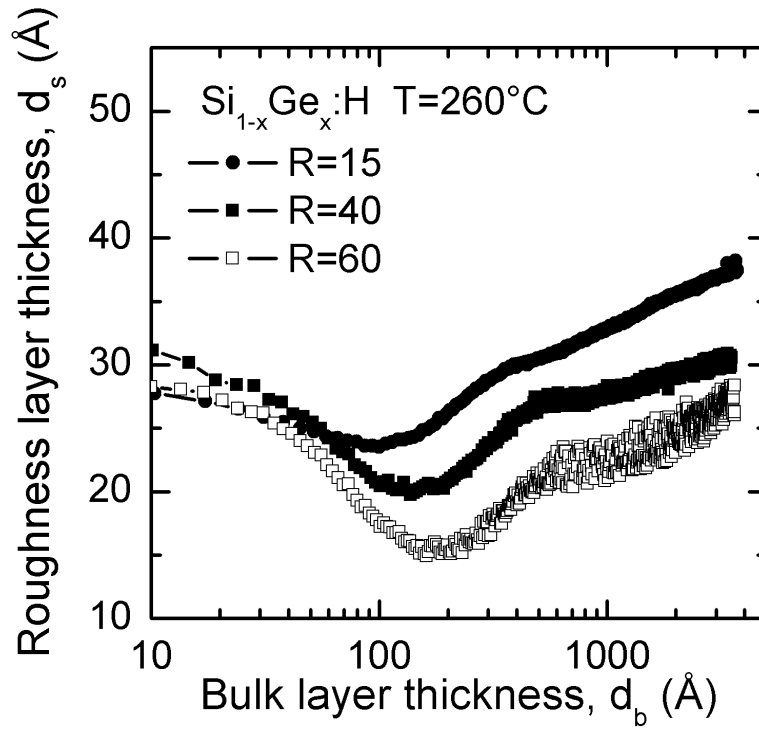


Figure 7: Surface roughness layer thickness versus bulk layer thickness for Si_{1-x}Ge_x:H films with $R = 15, 40$, and 60 deposited at low power (0.08 mW/cm^2) and low total pressure ($< 0.9 \text{ Torr}$) on native oxide-covered c-Si substrates held at 260°C .

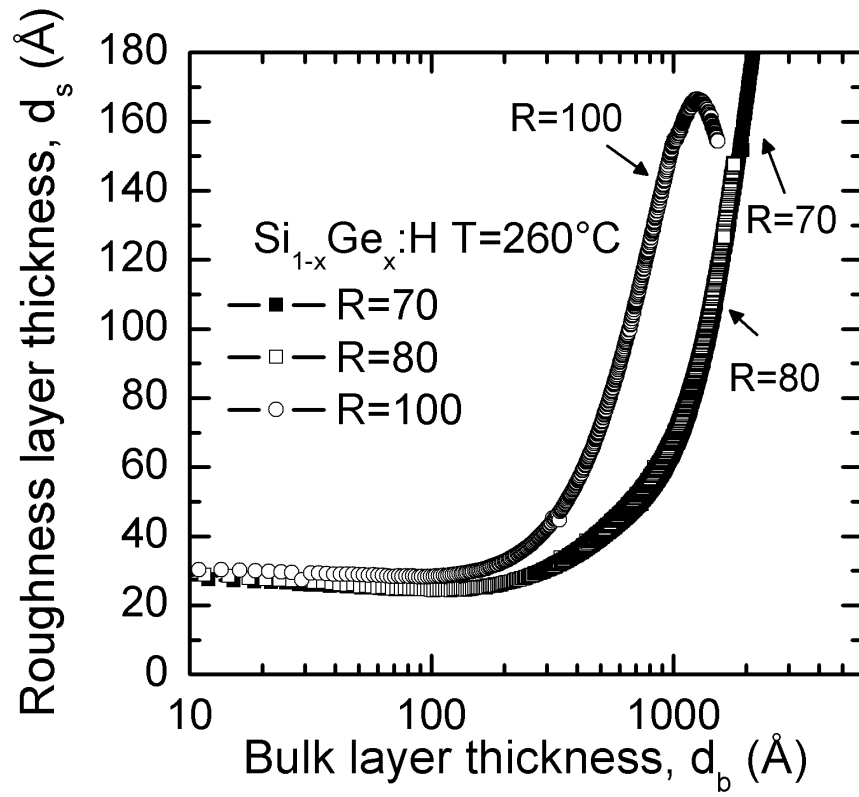


Figure 8: Surface roughness layer thickness versus bulk layer thickness for $\text{Si}_{1-x}\text{Ge}_x\text{:H}$ films with $R = 75, 80, 100$. For this series, the substrate temperature was 260°C , the plasma power was 0.08 mW/cm^2 , and the reactive gas partial pressure was between 0.03 and 0.09 Torr.

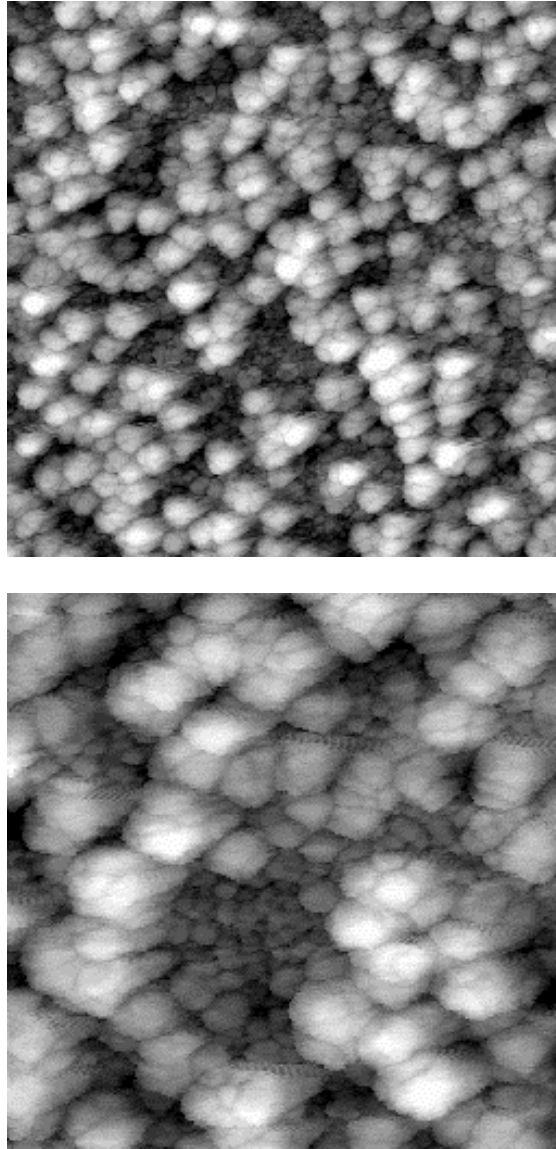


Figure 9: Atomic force microscopy images for an $R=80 \text{ Si}_{1-x}\text{Ge}_x\text{:H}$ film deposited on a native-oxide/c-Si substrate. The ($2 \mu\text{m} \times 2 \mu\text{m}$) (top) and ($1 \mu\text{m} \times 1 \mu\text{m}$) (bottom) images were obtained on the same film, having a bulk layer thickness of 1800 \AA , as deduced by RTSE

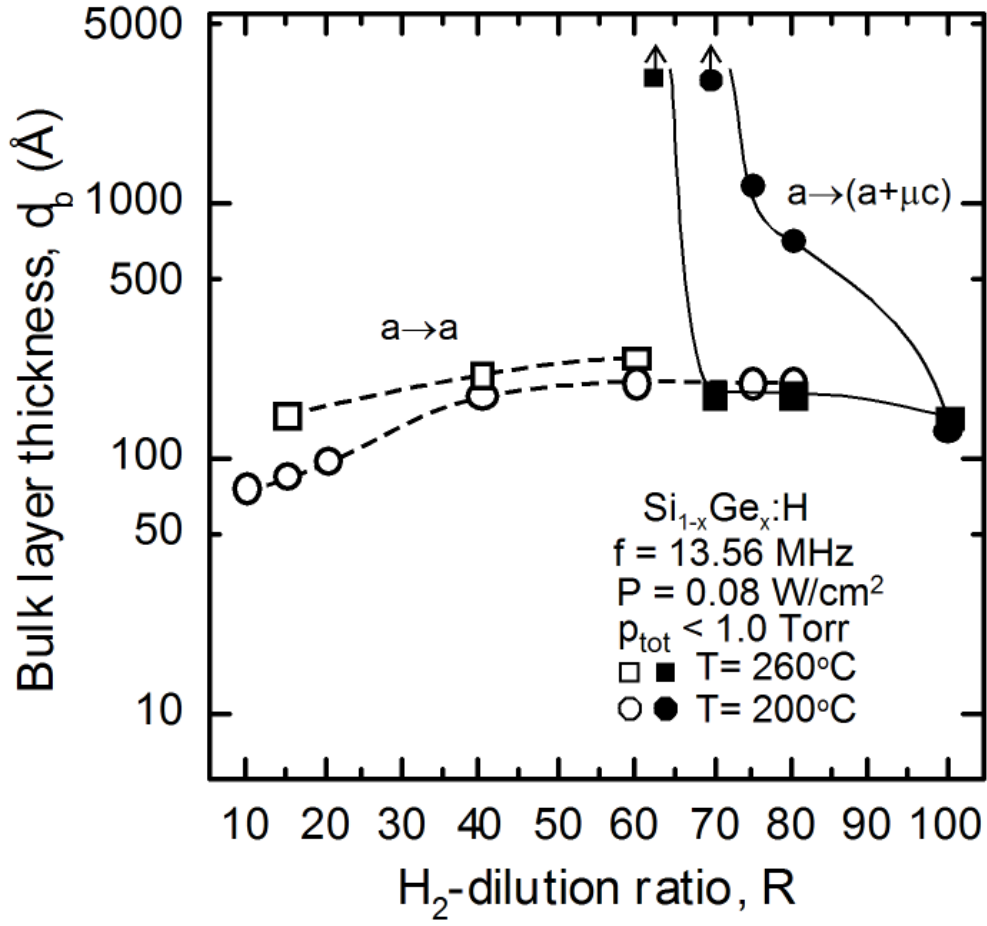


Figure 10: Superimposed phase diagrams for $Si_{1-x}Ge_x:H$ films deposited at two different substrate temperatures: $200^\circ C$ (circles) and $260^\circ C$ (squares). Both series were deposited on native oxide-covered c-Si substrates at low power (0.08 mW/cm^2) and low total pressure ($< 0.9 \text{ Torr}$). The up arrows indicate that the transition occurs (above) the designated value.

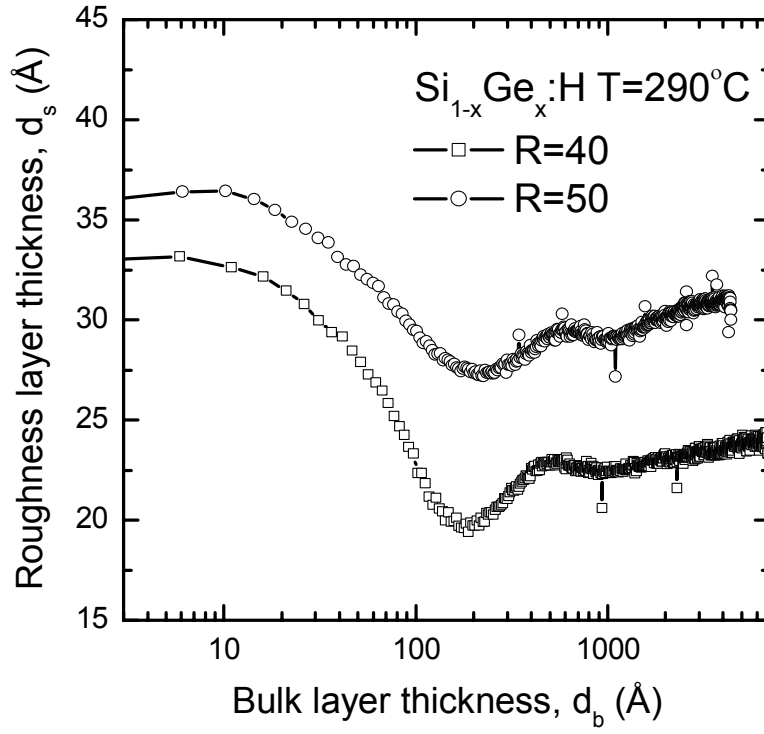


Figure 11: Surface roughness layer thickness versus bulk layer thickness for $\text{Si}_{1-x}\text{Ge}_x\text{:H}$ films with $R = 40$ and 50 deposited at low power (0.08 mW/cm^2) and low total pressure ($< 0.9 \text{ Torr}$) on native oxide-covered c-Si substrates held at 290°C .

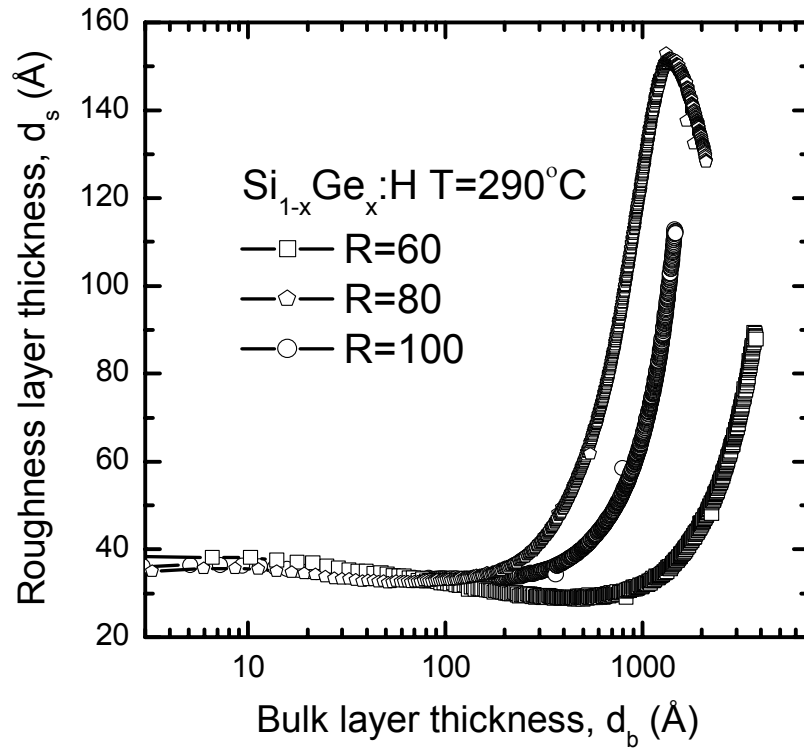


Figure 12: Surface roughness layer thickness versus bulk layer thickness for $\text{Si}_{1-x}\text{Ge}_x\text{:H}$ films with $R = 60, 80, 100$. For this series, the substrate temperature was 290°C , the plasma power was 0.08 mW/cm^2 , and the reactive gas partial pressure was between 0.03 and 0.09 Torr.

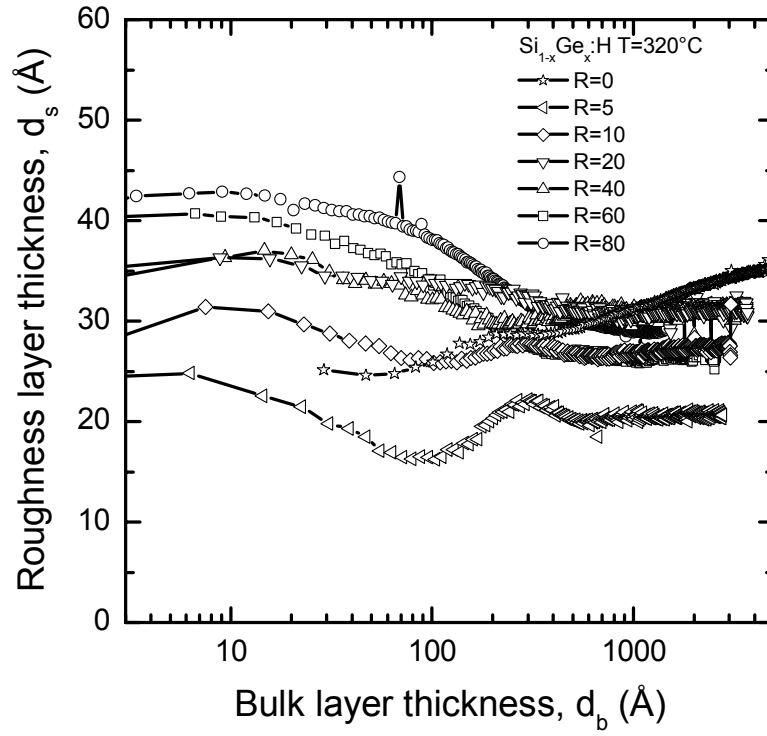


Figure 13: Surface roughness layer thickness versus bulk layer thickness for $\text{Si}_{1-x}\text{Ge}_x\text{:H}$ films with $R = 0, 5, 10, 20, 40, 60$, and 80 deposited at low power (0.08 mW/cm^2) and low total pressure ($< 0.9 \text{ Torr}$) on native oxide-covered c-Si substrates held at 320°C .

Task 3: Device loss mechanisms

Dark forward bias current, J_D -V, characteristics have been shown to be a new probe for characterizing carrier recombination, identifying the mechanisms limiting solar cell performance, as well as characterizing the defect states in the i-layers of a-Si:H solar cells]. From the bias dependence of the differential diode quality factors, $n(V)$, predictions can be made about the nature of the gap state distributions. The results obtained, in which carrier transport is clearly dominated by bulk recombination, show that there are distinct differences between the two types of i-layers in their distributions of both native and light induced defect states. It has also been reported that in such cell structures with protocrystalline i-layers similar degradation kinetics of J_D -V characteristics can be obtained with 1 sun illumination to that due to the recombination with dark forward bias currents corresponding to J_{sc} . Such “equivalence” has also been found will undiluted a-Si:H i-layers where this is illustrated with results of the J_D -V characteristics shown in Figure 14. More importantly this similarity also exists in the differential diode quality factors, $n(V)$, which are directly related to the corresponding energy distributions of the defect states in the i-layer, which is illustrated in Figure 15. This ability to create and directly characterize the metastable defect states with dark current voltage characteristics at the same temperatures greatly enhances the ability to characterize their creation as well as the changes in their subsequent relaxation. In addition a strong similarity is obtained not only in the changes of J_D -V and $n(V)$ characteristics but also in that of the fill factors as illustrated in Figure 16. In the experimental apparatus constructed under the present contract both J_D -V and FF measurements can be carried out at well controlled temperatures for direct correlation thus allowing direct information to be obtained not only about the nature of the metastable defects but also about their effects on the fill

factors. Such studies have been undertaken in identifying and quantifying the respective contributions of the fast and slow defect states utilizing carrier recombination from dark currents which correspond to 1 sun J_{sc} but also at far forward biases that correspond to high intensity illuminations.

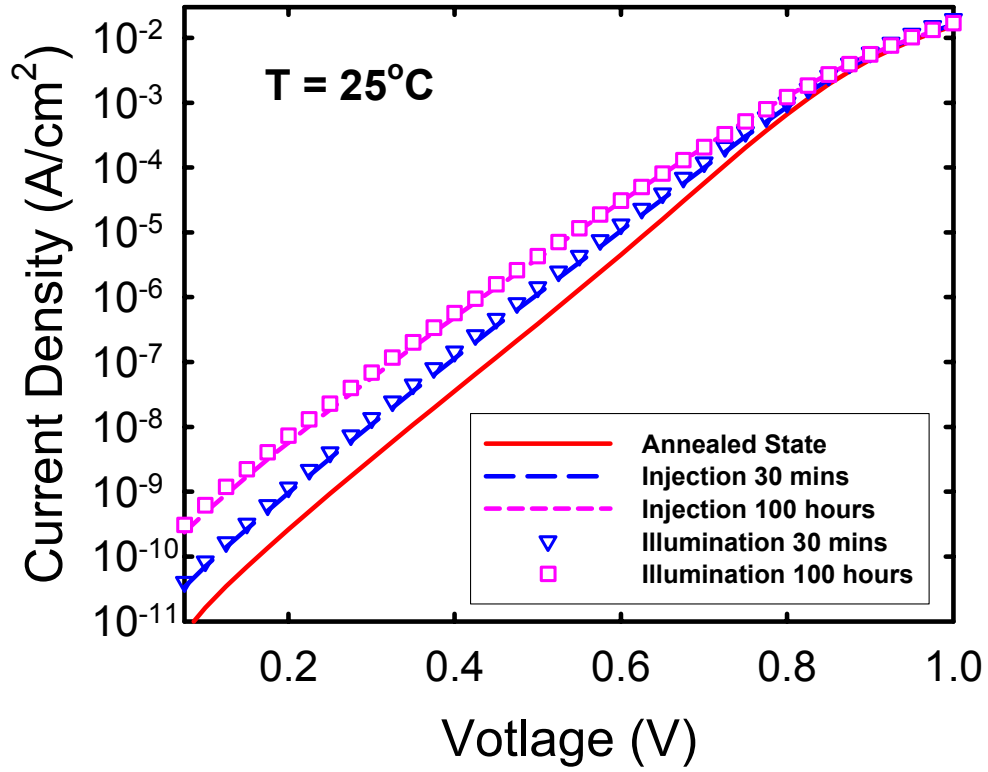


Figure 14: J_D -V characteristics for a p-i-n cell with $0.4\ \mu\text{m}$ thick $R=0$ bulk i-layer and $200\ \text{\AA}$ $R=40$ p/i interface layer at annealed state and after both 1 sun illumination and carrier injection induced degradation. The total recombination current in the case of the carrier injection is equal to J_{sc} of the cell under 1 sun illumination at the annealed state.

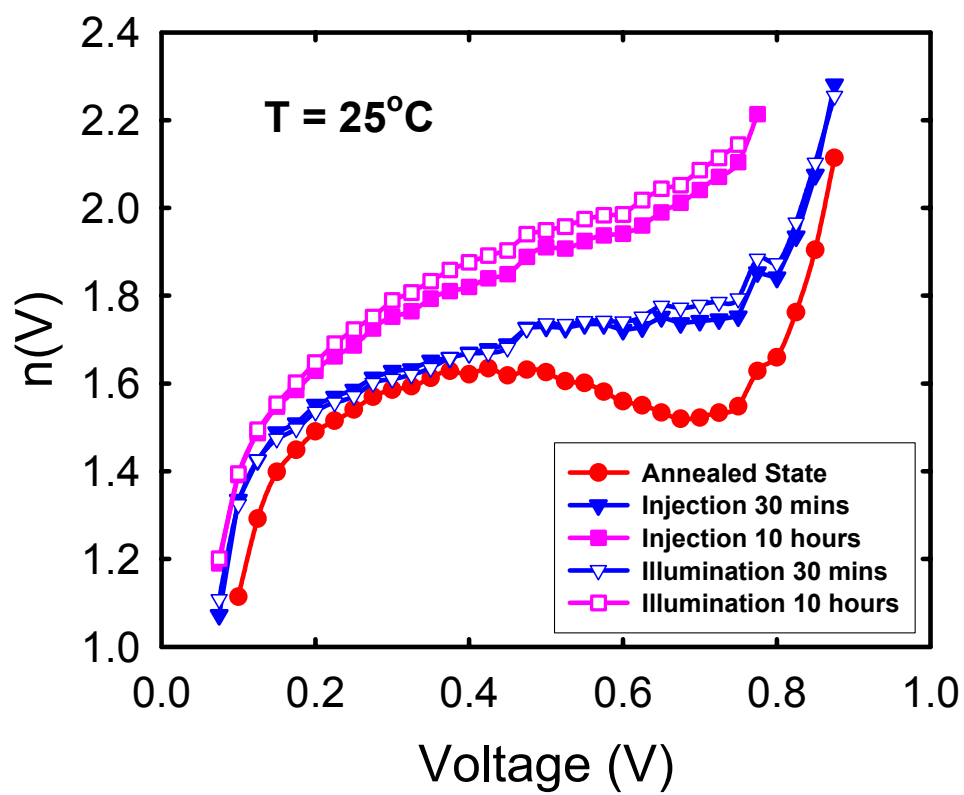


Figure 15: Corresponding $n(V)$ characteristics for Figure 14.

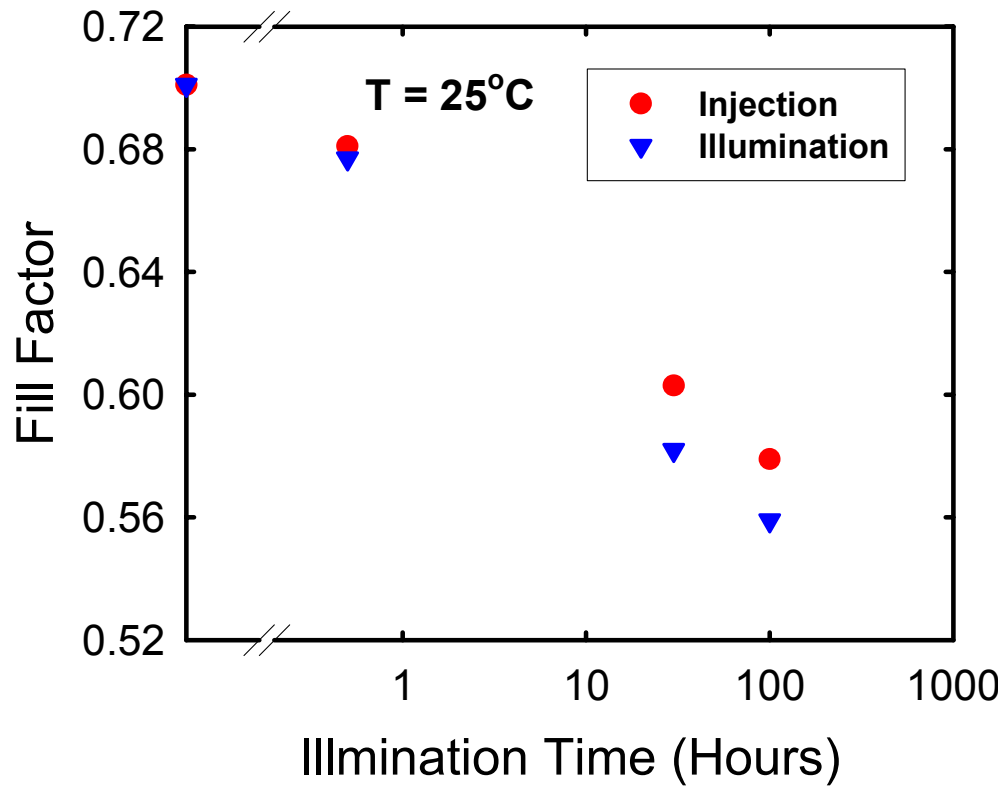


Figure 16: Degradation of fill factor with 1 sun illumination and carrier injection for the cell of Figure 14. The total recombination current in the case of the carrier injection is equal to J_{sc} of the cell under 1 sun illumination at the annealed state.

Task 4: Characterization Strategies for Advanced Materials

A detailed study has been undertaken of the relaxation of light induced changes in a-Si:H films after 1 sun illumination first observed and being studied in p-i-n solar cell structures. This is being carried out on both diluted protocrystalline and undiluted a-Si:H films on an experimental station which allows the sample temperatures as well as illumination levels to be closely and reproducibly controlled. In addition close attention has been given to obtaining reliable and reproducible results in both the kinetics of light induced changes as well as their relaxation. This has been achieved with experiments that are carried out on an experimental station which is computer controlled and allows photocurrents to be continuously measured as a function of time. This has greatly improved the ability to accurately characterize the photocurrents as well as allowing multiple experiments to be carried out in a controlled way. This is illustrated in Figure 17 where the results of the photocurrents obtained during 1 sun illumination, are shown for a protocrystalline film where it has been degraded and subsequently annealed four times. In these results where the 1 sun illumination has undergone a sequence of interruptions for 7 seconds, the ensuing subsequent relaxations can be clearly seen as well as the dependence on the time of illumination. In Figure 18 a generation rate of $5 \times 10^{15} \text{ cm}^{-3} \text{ s}^{-1}$ is used to produce both the photocurrent obtained during the recovery after 30 minutes of 1 sun illumination, but also the subsequent recoveries after their erasure to the same photocurrent obtained in the initial degraded state. The careful measurements being carried out on protocrystalline a-Si:H have revealed differences between the relaxation obtained for films that were deposited under the same conditions but at different times. These differences are being investigated to identify their cause and to establish the characteristics that can be reliably related to the results from those on the i layers of solar cells. In parallel studies, the long term relaxation

in the subgap absorption has been clearly observed and is being investigated to obtain additional information about the nature of the fast and slow states from the changes in the two distributions of light induced defects previously identified.

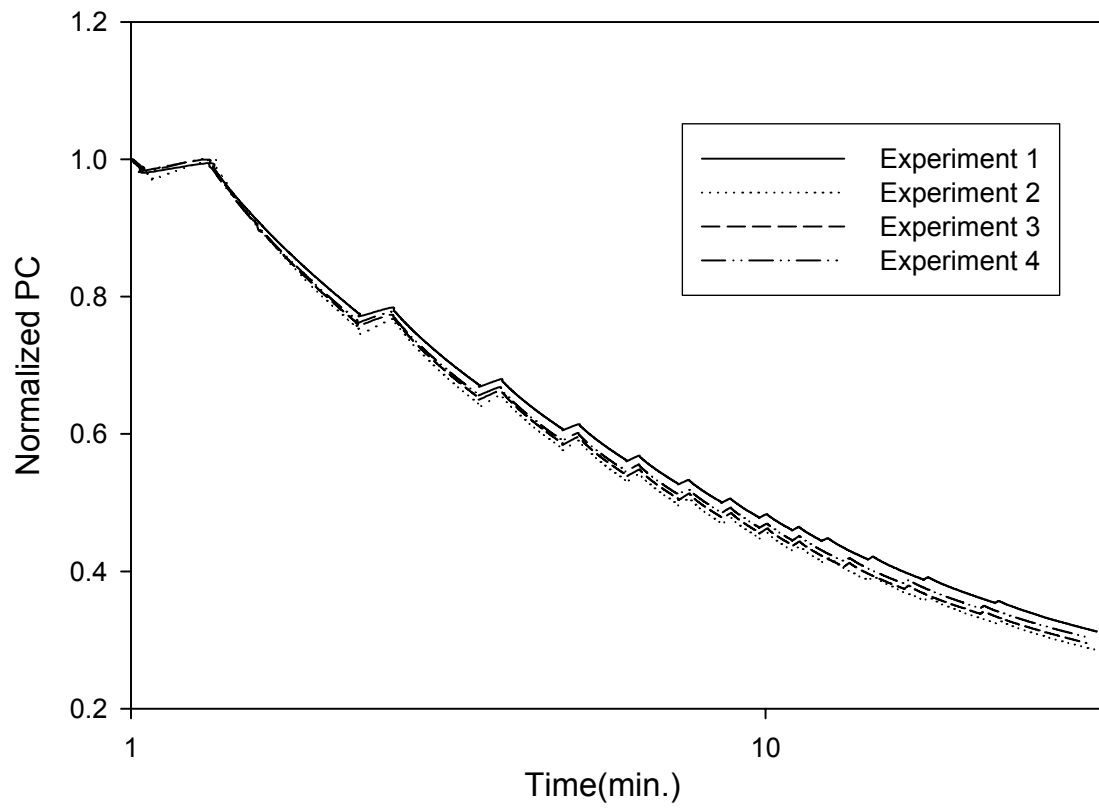


Figure 17: Normalized photocurrents during 1 Sun degradation on the same R=10 a-Si:H film. The 8000 angstrom thick sample was thermally annealed at 170°C for 4 hours prior to being subjected to 1 sun degradation.

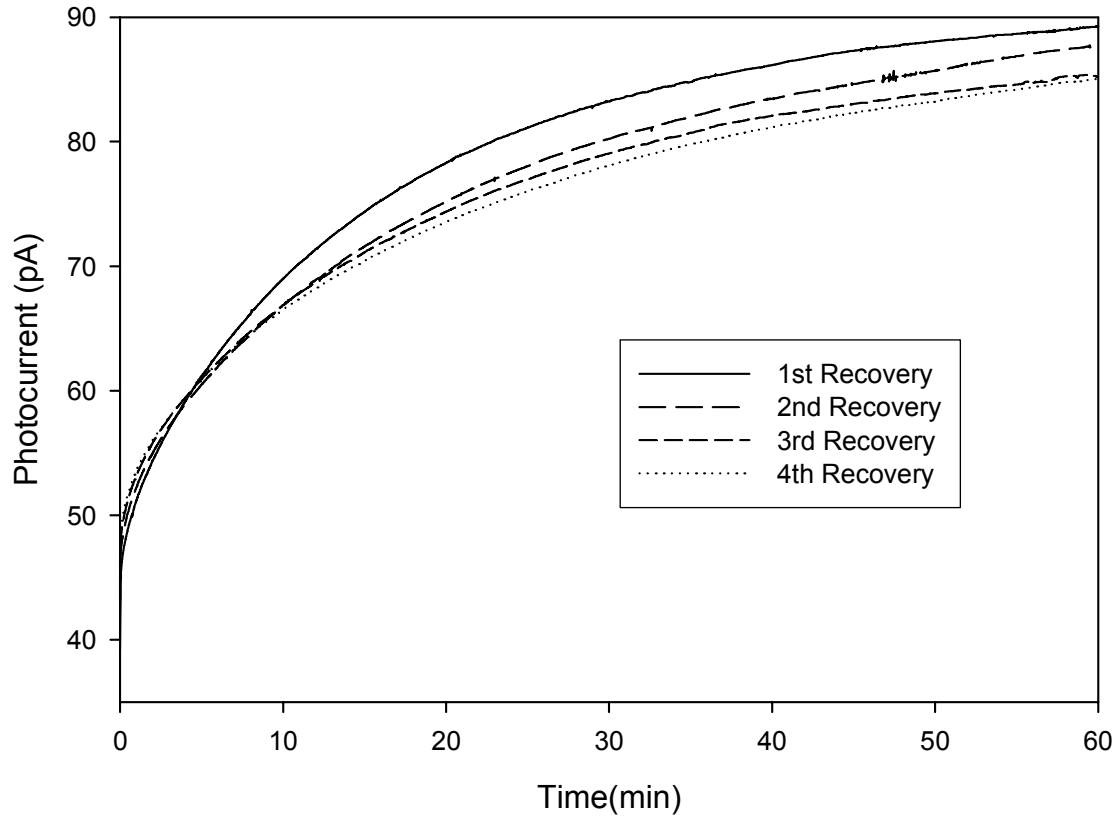


Figure 18: Photocurrents with a carrier generation rate of $10^{16} \text{ cm}^{-3}\text{s}^{-1}$ for multiple relaxations of an R=10 a-Si:H film after 1 sun degradation at 25°C. The first recovery follows a 30min. 1 sun exposure. Subsequent recoveries follow a 1 sun exposure to degrade the sample to the same degraded state photocurrent attained in the first degradation.